



Available online at www.sciencedirect.com

ScienceDirect

Advances in Space Research 72 (2023) 1208–1223

**ADVANCES IN
SPACE
RESEARCH**
(*a COSPAR publication*)
www.elsevier.com/locate/asr

Earth's magnetotail variability during supersubstorms (SSSs): A study on solar wind–magnetosphere–ionosphere coupling

Rajkumar Hajra ^{a,*¹}, Ezequiel Echer ^b, Adriane Marques de Souza Franco ^c
Mauricio José Alves Bolzan ^d

^a Indian Institute of Technology Indore, Simrol, Indore 453552, India

^b Instituto Nacional de Pesquisas Espaciais (INPE), São José dos Campos, Brazil

^c Federal University of Southern and Southeastern Pará, Marabá, Brazil

^d Federal University of Jataí, Jataí, Brazil

Received 6 July 2022; received in revised form 19 March 2023; accepted 7 April 2023

Available online 17 April 2023

Abstract

Supersubstorm (SSS) events are associated with extremely intense westward auroral electrojet currents (the minimum SuperMAG AL or SML < -2500 nT) resulting from the solar wind-magnetosphere coupling. We present, for the first time, variability of the Earth's magnetotail and coupling from the solar wind to magnetotail, geosynchronous orbit and auroral ionosphere during the SSS events. Five intervals with multiple SSSs were identified when the *Cluster* spacecraft was well inside the inner magnetotail. The SSS events are found to be characterized by turbulent magnetotail plasma sheet and injection of energetic (~ 100 eV to ~ 100 keV) electrons and protons. Injection of energetic protons from the plasma sheet causes electromagnetic ion cyclotron waves that lead to pitch angle scattering of the outer radiation belt MeV electrons and loss to the atmosphere during the SSSs. The SSS events are found to be associated with interplanetary magnetic clouds characterized by slowly varying interplanetary magnetic fields. An overall overall increase in the turbulence is recorded from the solar wind to the inner magnetosphere-ionosphere system during the SSSs. From the wavelet and cross-wavelet analyses, the inner magnetosphere and ionosphere are found to respond quasi-periodically at $\sim 1.5 - 4$ hours, and sporadically at shorter timescales of $\sim 0.5 - 1.5$ hours.

© 2023 COSPAR. Published by Elsevier B.V. All rights reserved.

Keywords: Supersubstorms; Magnetic reconnection; Interplanetary magnetic field; Magnetic cloud; Geomagnetic disturbances; Magnetotail

1. Introduction

During magnetospheric substorms (Akasofu, 1964; Rostoker et al., 1980; Baker et al., 1996; Liou et al., 2001; Østgaard et al., 2005) solar wind kinetic energy is injected into the Earth's magnetotail and released

subsequently in the auroral ionosphere. The general physical scenario is as follows. Dayside magnetic reconnection (Dungey, 1961) between the interplanetary magnetic field (IMF) southward component [B_s] and northward geomagnetic field, followed by downtail transport of the “open” magnetic field lines across the polar cap by the solar wind flow causes injection of the energetic electrons and ions into the Earth's magnetotail (Tsurutani and Meng, 1972). External triggers like interplanetary shocks impinging on the magnetosphere can release this energy in form of a substorm in the midnight sector (Akasofu and Chao, 1980; Meurant et al., 2005; Tsurutani et al., 2011). Zhou and

* Corresponding author.

E-mail addresses: rajkumarhajra@yahoo.co.in, rhajra@ustc.edu.cn (R. Hajra).

¹ Now at CAS Key Laboratory of Geospace Environment, School of Earth and Space Sciences, University of Science and Technology of China, Hefei, People's Republic of China

Tsurutani (2001) reported the midnight sector substorm onsets within ~ 2 minutes after the shock arrival. It was suggested that the energy for the shock-induced substorms could be provided by precursor IMF B_s up to ~ 1.5 hours prior to the shock arrival. The substorm-injected energetic ($\sim 1 - 100$ keV) electrons deposit their energy in the ~ 160 km to ~ 75 km altitude range, depending on their energy (see Rees, 1963; Rees, 1964; Semeter and Kamalabadi, 2005; Jones et al., 2009; Fang et al., 2010; Artamonov et al., 2016; Tsurutani et al., 2019, and references therein). The precipitating electrons may lead to two types of electron auroras: discrete auroras associated with energetic $\sim 1 - 10$ keV electron precipitation (e.g., Swift, 1978; Carlson et al., 1998), and diffuse auroras associated with $\sim 10 - 100$ keV electron precipitation (e.g., Meng et al., 1979; Thorne et al., 2010).

Based on a large number of auroral all-sky images, Akasofu (1964) proposed “a working model” of auroral evolutions during a substorm. Accordingly, a substorm onset is indicated by an auroral brightening in a localized region of the equatorward-most midnight sector arc, followed by its expansion to the west, east and poleward directions in the expansive phase. In the recovery phase, the arc exhibits equatorward motion, and the auroral brightness reduces considerably. The westward component of the auroral electrojet current flowing at ~ 100 km altitude peaks in the region of the brightest aurora (e.g., Rostoker et al., 1980).

The substorm related intense, westward auroral electrojet current is measured by the SuperMAG AL or SML indices. A subset of the substorms with the SML peak intensity (the SML minimum) < -2500 nT was defined as supersubstorms (SSSs) by Tsurutani et al. (2015). SSSs were suggested to be isolated events associated with precursor IMF B_s , and externally triggered by solar wind plasma parcels with high density (ram pressure) impinging on the magnetosphere (Hajra et al., 2016). Statistically, the B_s fields were shown to be part of interplanetary magnetic clouds (MCs) in 46% and of interplanetary sheath fields in 54% of the cases (Hajra et al., 2016; Despirak et al., 2019). However, Hajra and Tsurutani (2018a) reported two SSS events triggered by interplanetary shocks, where the computed precursor energy input through magnetic reconnection was insufficient to account for the large ionospheric energy dissipation. Additional direct driving through magnetic reconnection and solar wind ram energy were argued to be important during the SSSs. Recently, Tsurutani and Hajra (2023) conducted a detailed study on the solar wind energy input and dissipation in the magnetospheric-ionospheric system for 17 shock-triggered SSSs during solar cycles 23 and 24. The shock compression was shown to greatly strengthen the upstream B_s , thus enhancing the solar wind energy input into the magnetosphere and ionosphere (through magnetic reconnection) during the SSS events. The additional solar wind magnetic reconnection energy input is suggested to supplement the ~ 1.5 -hour precursor (growth phase) energy input, both

supplying the necessary energy for the high-intensity, long-duration SSS events. The major part of the solar wind input energy was found to be dissipated into Joule heating ($\sim 30\%$), with substantially less energy dissipation in auroral precipitation ($\sim 3\%$) and in ring current energy ($\sim 2\%$). It was found that during the SSS events the day-side Joule heating is comparable to that of the night-side Joule heating, giving a picture of a global energy dissipation in the magnetospheric/ionospheric system, not simply a night-side sector substorm effect. In addition, the SSSs are shown to have a different auroral evolution than a nominal Akasofu-type substorm. In contrast to the standard midnight substorm onset and following expansion, SSSs were shown to exhibit premidnight and postmidnight intense auroras, with the midnight sector devoid of intense auroras (Hajra and Tsurutani, 2018a). All these results clearly indicate the distinguishing features of the SSS events compared to nominal substorms, and call for further exploration in order to better understand the events.

In this present work, we will study the variability of the magnetotail during the SSSs for the first time. The evolution of the turbulence from the solar wind to the inner magnetotail and auroral ionosphere will be explored. By inner magnetotail, we refer to geocentric distances ≤ 20 Earth radii (R_E). The SSS variability in this region is particularly interesting. During a substorm growth phase, a thin current sheet develops near the planet, and the cross-tail currents are intensified. This is followed by release of the accelerated particles due to the magnetic stress caused in this region due to that transition (Lui, 2000). In addition, we will study the periodic response of the magnetotail and ionosphere to the solar wind forcing. This will hopefully augment our understanding of the solar wind-magnetotail-ionosphere energy coupling during the SSSs.

2. Database and methods of analysis

2.1. Database

This multi-instrument study makes use of the solar wind measurements in the interplanetary space upstream of the Earth, the magnetotail plasma, magnetic field and wave measurements, the relativistic electron flux measurements at the geosynchronous orbit, and the ground-based magnetic field measurements.

The upstream solar wind plasma and IMF data at 1 minute time resolution are collected from NASA’s OMNI database (<http://omniweb.gsfc.nasa.gov/>). These are based on multi-spacecraft measurements, shifted to the Earth’s bow shock nose. The IMF vector components in *geocentric solar magnetospheric* (GSM) coordinates are used, in which the x -axis is directed towards the Sun and the y -axis is in the $\Omega \times \hat{x} / |\Omega \times \hat{x}|$ direction, where Ω is aligned with the geomagnetic dipole axis, \hat{x} is the unit vector along the x -axis. The z -axis completes a right-hand system.

The variability of the Earth's inner magnetotail is studied by observations made by the *Cluster* (Escoubet et al., 1997) spacecraft of the European Space Agency (ESA; <https://www.cosmos.esa.int/web/csa/access>). For this purpose, we have considered the *Cluster* 1 passes at $> 5R_E$. Geomagnetic field (GMF) is measured at a resolution of ~ 4 seconds by the *FluxGate Magnetometer* (FGM; Balogh et al., 1997). The *Cluster* 1 position and magnetic field measurements are considered in the *geocentric solar ecliptic* (GSE) coordinate system, which is identical to the GSM system except by a rotation about the x -axis. The > 30 keV electron and proton spectrograms are obtained from the *Research with Adaptive Particle Imaging Detectors* (RAPID; Wilken et al., 1997). The spectrograms of the lower energy electrons (0.6 eV–26 keV) and protons (0.5 eV–32 keV) are obtained from the *Plasma Electron and Current Experiment* (PEACE; Johnstone et al., 1997) and the *Cluster Ion Spectrometry* (CIS; Rème et al., 1997), respectively. The magnetic field spectrograms are obtained from the *Spatio-Temporal Analysis of Field Fluctuations* (STAFF; Cornilleau-Wehrlin et al., 1997) experiment on board *Cluster*.

The integrated fluxes of relativistic > 0.6 and > 2.0 MeV electrons are collected from the *Geostationary Operational Environment Satellites* 12 (GOES 12; <http://www.ngdc.noaa.gov/stp/satellite/goes/dataaccess.html>) at geosynchronous orbit ($L = 6.6$). The electron fluxes, measured by solid-state detectors with pulse height discrimination in the energetic particle sensors, are corrected for secondary responses from other energies (e.g., protons > 32 MeV) and from directions outside the nominal detector entrance apertures (Onsager et al., 1996).

The geomagnetic SYM-H index, considered a proxy for equatorial ring current strength (Wanliss and Showalter, 2006; Iyemori et al., 2010), is used to study the instantaneous magnetic storm condition (Gonzalez et al., 1994). The 1 minute resolution SYM-H index is obtained from the *World Data Center for Geomagnetism*, Kyoto, Japan (<http://wdc.kugi.kyoto-u.ac.jp/>). The SSS onset, strength, and duration are studied by the geomagnetic SML index (1 minute) obtained from the SuperMAG website (<https://supermag.jhuapl.edu/>). The SML index, representing the westward auroral electrojet current, is based on magnetic observations by a global network of ~ 300 ground-based magnetometers (Gjerloev, 2009; Gjerloev, 2012; Newell and Gjerloev, 2011a; Newell and Gjerloev, 2011b).

2.2. Methods of analysis

From the SML index temporal variation, a substorm is identified as an interval of a sharp decrease in SML leading to a negative bay development and followed by the bay recovery to pre-substorm values (Newell and Gjerloev, 2011a). An event with the SML minimum < -2500 nT is defined as an SSS (Tsurutani et al., 2015). We identified all SSSs when suitable *Cluster* spacecraft measurements

are available inside the magnetotail ($> 5R_E$). These are listed in Table 1.

Fourier transform is applied to the solar wind, magnetospheric and ionospheric parameters to study the turbulence in these regions. The Fourier spectrum of the time series is fitted with a power law function as: $P = cf^\alpha$, where P is the Fourier spectral power, c is a constant, f is the frequency and α is the power law index. This method is widely used in turbulence studies to characterize the plasma wave activity, as well as in turbulence dependent on the system scales or frequencies of oscillations in the system (Bailey and Swarztrauber, 1994; Bracewell, 2014).

Wavelet transform (WT) is an useful tool to study the non-stationary (time dependent) variations, such as those observed in the solar wind-magnetosphere-ionosphere system. We use the Morlet wavelet function (Torrence and Compo, 1998) in order to identify the significant periodic variations in the solar wind, inner magnetotail, and the auroral ionospheric parameters under this study. In addition, cross-wavelet transform (XWT), that provides a dynamic energy correlation between two time series (see, e.g., Bolzan and Rosa, 2012), is used to quantify relationships among the three regions. The global wavelet spectrum (GWS) is used to specify the most energetic periods present in the WT and XWT analyses. For detailed definitions, descriptions and examples of these techniques applied to space research, we refer the reader to previous works (e.g., Morettin, 2014; Souza et al., 2016; Souza et al., 2018; Hajra et al., 2021).

3. Results and discussion

3.1. Case study of SSSs during day 209 of year 2004

Fig. 1 shows an example of SSS events occurring during day 209 (27 July) of year 2004. The SML peaks < -2500 nT and corresponding times are listed in Table 1 and the same are marked by red vertical solid lines in the figure. From the SYM-H index variation (Fig. 1i), the SSS events are found to occur during the multi-step main phase of a super geomagnetic storm with the SYM-H peak of -208 nT at $\sim 13:38$ UT on day 209 (Gonzalez et al., 1994). During the SSS events, the *Cluster* 1 spacecraft was well inside the magnetotail (at $< -15R_E$) (Fig. 1a, Table 1).

From the solar wind plasma and IMF measurements at the dayside bow shock nose, the interval is found to be characterized by a fast forward (FF) shock followed by an interplanetary sheath and a flux rope MC. These are associated with the interplanetary counterpart of a fast (speed ~ 1333 km s $^{-1}$) halo coronal mass ejection (CME) erupted from the Sun at $\sim 14:54$ UT on day 207 or an interplanetary CME (ICME). The details of the halo CME can be found in the SOHO/LASCO catalog (https://cdaw.gsfc.nasa.gov/CME_list/halo/halo.html). The FF shock is marked by a vertical black dashed line at $\sim 22:48$ UT on day 208 (FF₂₀₈), ~ 32 hours after the eruption of the halo

Table 1
Details of the events selected for this study.

Event	SSS SML peak	SSS peak time	Driver	Cluster at SSS peak	Cluster orbit ($> 5 R_E$)	
	(nT)	(UT/DOY)		(R_E)	Start	End
2001_310	-2839	04:04/310	ICME ¹	-9.67	13:28/309	22:20/310
2003_302	-2729	22:41/302	MC ¹	-7.71	19:34/302	06:14/304
	-3872	20:03/303	MC ¹	-9.56		
	-2724	21:32/303	MC ¹	-9.11		
2004_209	-2933	08:33/209	MC	-15.18	12:03/208	04:38/210
	-2534	09:25/209	MC	-15.18		
	-2528	10:16/209	MC	-15.13		
	-2901	12:45/209	MC	-14.82		
2004_313	-2831	04:06/313	MC	-7.42	00:19/313	05:07/314
	-2564	10:11/313	MC	-8.87		
2005_236	-4143	10:18/236	MC	-17.83	15:41/235	09:29/237
	-4017	10:37/236	MC	-17.85		

¹ Gap in high-resolution data, possible drivers reported in Richardson and Cane (2010) are listed.

CME at the Sun. Detailed characteristic parameters of FF₂₀₈ are listed in Table 2. FF₂₀₈ is characterized by abrupt and large increases in solar wind speed [V_{sw}] (from ~ 607 to $\sim 937 \text{ km s}^{-1}$, Fig. 1c), plasma density [N_{sw}] (from ~ 2.0 to $\sim 6.9 \text{ cm}^{-3}$, Fig. 1d, black), ram pressure [P_{sw}] (from ~ 1.4 to $\sim 5.9 \text{ nPa}$, Fig. 1d, red), temperature [T_{sw}] (from $\sim 1.4 \times 10^5$ to $\sim 9.3 \times 10^5 \text{ K}$, Fig. 1e, black), and IMF magnitude [B_0] (from ~ 1.6 to $\sim 10.3 \text{ nT}$, Fig. 1f) (Landau and Lifshitz, 1960; Kennel et al., 1985; Tsurutani et al., 2011). Using the plasma-IMF mixed-mode method (Abraham-Shrauner and Yun, 1976) and the Rankine–Hugoniot conservation equations (Rankine, 1870; Hugoniot, 1887; Hugoniot, 1889), FF₂₀₈ is found to have a magnetosonic Mach number [M_{ms}] of ~ 5.3 and a shock normal angle [θ_{Bn}] of $\sim 64^\circ$ relative to the upstream magnetic field (see Smith, 1985; Tsurutani and Lin, 1985, for detail description of the shock analysis). The shock caused a sudden impulse [SI⁺] of $\sim 77 \text{ nT}$ in the SYM-H index (Fig. 1i), and triggered a substorm with the SML and SME peaks of -1586 and 2336 nT , respectively at $\sim 23:46 \text{ UT}$ on day 208.

The shock was followed by an interplanetary sheath from $\sim 22:48 \text{ UT}$ on day 208 to $\sim 02:53 \text{ UT}$ on day 209 (sh₂₀₈). This is marked by a green bar on the top of Fig. 1. The sheath is characterized by compressed and turbulent plasma, largely fluctuating IMF (Kennel et al., 1985; Tsurutani and Lin, 1985; Tsurutani et al., 1988), with a peak southward component of -20.2 nT (Fig. 1f). The consequent magnetic reconnection caused the energy driving for the above-mentioned substorm (Fig. 1g–h), and a ring current enhancement leading to the SYM-H peak of -126 nT at $\sim 02:04 \text{ UT}$ on day 209 (Fig. 1i). During the passage of the sheath, GMF inside the magnetotail also exhibited large fluctuations (Fig. 1b).

An MC (shown by a vertical shading and a red horizontal bar on the top of Fig. 1) followed the sheath and continued up to $\sim 16:10 \text{ UT}$ on day 209 (MC₂₀₉). MC₂₀₉ is identified from a low T_{sw} ($\sim 0.3 \times 10^5 \text{ K}$, Fig. 1e, black) and a low plasma-beta [β] (~ 0.02 , Fig. 1e, red). Smooth

rotations in the IMF B_x , B_y and B_z components (Fig. 1f) are indicative of a giant flux rope (Burlaga et al., 1981; Klein and Burlaga, 1982). During MC₂₀₉, IMF was characterized by a long-duration (~ 11 hours) southward component with a peak intensity of -22 nT . This supplied the energy for the SSSs. The magnetotail GMF was largely compressed (with a peak GMF B_0 of 89.2 nT) and fluctuating during MC₂₀₉ (Fig. 1b). The positive and negative values of the GMF B_x correspond to the northern and southern plasma sheet regions, respectively.

Fig. 2 shows variations of the geosynchronous orbit $\sim \text{MeV}$ electrons, along with the magnetotail plasma and wave activity during the SSSs shown in Fig. 1. The SML variation and the markings of the major interplanetary events (shock, sheath, and MC) are repeated from Fig. 1 for reference.

Energy spectrograms in Fig. 2 show injections of electrons ($\sim 100 \text{ eV}$ to $\sim 100 \text{ keV}$, Fig. 2c–d) and protons (~ 1 to $\sim 1000 \text{ keV}$, Fig. 2e–f) during the substorms. The SML peaks (Fig. 2a) are well-correlated with enhanced plasma fluxes injected into the magnetotail. Temperature anisotropies of the substorm-injected ~ 1 to $\sim 100 \text{ keV}$ electrons and protons lead to electromagnetic chorus waves (frequency: $\sim 100 \text{ Hz}$ to $\sim 10 \text{ kHz}$) (Kennel and Petschek, 1966; Tsurutani et al., 1979) and electromagnetic ion cyclotron (EMIC) waves (frequency: ~ 0.1 – 5 Hz) (Cornwall, 1965; Kennel and Petschek, 1966; Vasyliunas, 1976), respectively. The GMF spectrograms are shown separately in the ~ 0.6 – 10 Hz (Fig. 2h) and ~ 10 – 2000 Hz (Fig. 2g) frequency ranges to explore the wave activity. Triggered by the fast forward shock FF₂₀₈ (shown by the vertical dashed black line), the EMIC waves are observed during the entire interval of the substorm events (Fig. 2h). However, the wave activity above $\sim 100 \text{ Hz}$ (chorus waves) is comparatively lower (Fig. 2g) than that in the ~ 0.6 – 10 Hz range (EMIC). This is consistent with higher fluxes of ~ 1 – 100 keV protons (Fig. 2e) than the electron fluxes in the same energy range (Fig. 2c). The pitch angle distributions of the electrons and protons were also analyzed (not

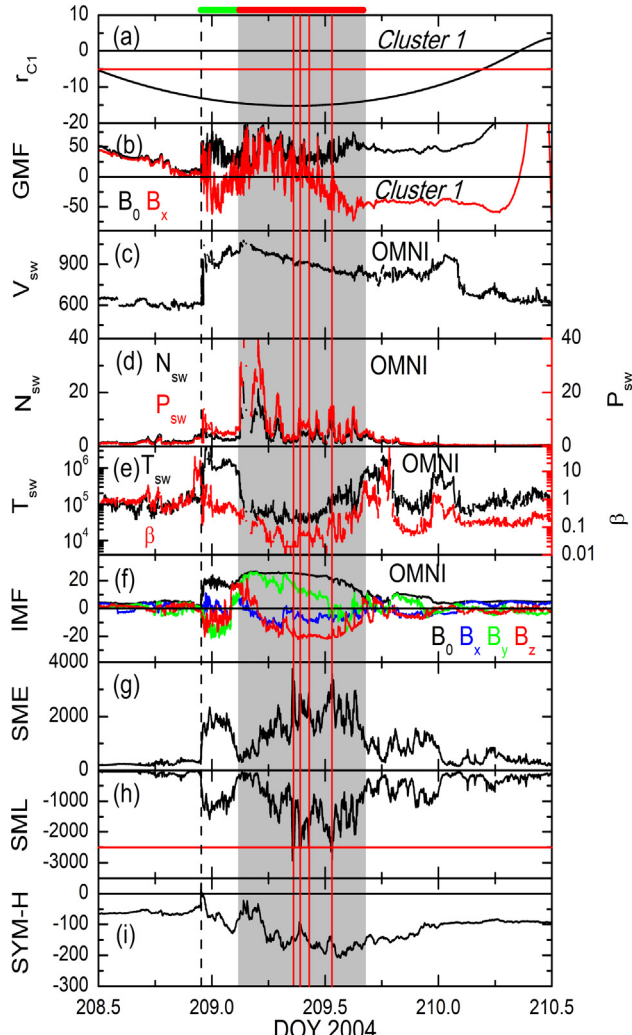


Fig. 1. Solar wind and interplanetary parameters during the SSS events on day 209 of year 2004. From top to bottom, the panels are (a) the *Cluster 1* spacecraft radial distance from Earth r_{C1} (R_E), (b) geomagnetic field (GMF) magnitude B_0 (nT, black) and B_x (nT, red) component along the *Cluster 1* orbit, (c) solar wind plasma speed V_{sw} (km s^{-1}), (d) density N_{sw} (cm^{-3} , black, legend on the left) and ram pressure P_{sw} (nPa, red, legend on the right), (e) temperature T_{sw} (K, black, legend on the left) and plasma β (red, legend on the right), (f) interplanetary magnetic field (IMF) magnitude B_0 (nT, black) and B_x (nT, blue), B_y (nT, green), B_z (nT, red) components at the Earth's bow shock nose, (g) geomagnetic SME (nT), (h) SML (nT) and (i) SYM-H (nT) indices, respectively during days 208–210 of year 2004. Red horizontal line in panel (a) shows the interval when *Cluster 1* was at $< -5R_E$, red horizontal line in panel (h) marks the SML $< -2500 \text{ nT}$ level. Vertical lines indicate the time of a fast forward shock (black dashed line), and the SSS SML peaks (red solid lines). Shaded region shows a magnetic cloud (MC) interval. Green and red horizontal bars on the top show the interplanetary sheath and MC, respectively.

shown) to understand the resultant wave activity. The energetic ($\sim 1 - 100 \text{ keV}$) protons are found to exhibit isotropic distribution, showing pitch angles uniformly between 0° and 180° , and strong fluxes during the entire interval of the interplanetary sheath and MC, while the energetic electrons exhibited isotropic distributions only for short intervals, and their fluxes were comparatively less. It may be noted that a detail inspection of the $\sim 10 - 2000 \text{ Hz}$ magnetic field spectrum reveals the distinct waves rising in fre-

quency in the range of $0.1f_{ce} < f < f_{ce}$ (where f_{ce} is the local electron gyrofrequency) are chorus waves, and not plasmaspheric hiss, the latter being a structureless/steady, incoherent noise or broadband emission (Thorne et al., 1973; Hayakawa et al., 1986; Tsurutani et al., 2015).

Variations of the relativistic > 0.6 and $> 2.0 \text{ MeV}$ electrons in the geosynchronous orbit (Fig. 2b) show that fluxes of the $\sim \text{MeV}$ electrons decreased sharply with the shock impingement on the magnetosphere. In addition, the $\sim \text{MeV}$ electron fluxes were fluctuating but lower during the substorm occurrence interval compared to the pre- and post-substorm periods. However, short-term flux enhancements are recorded to be co-incident with the SSS SML peaks (Fig. 2a). While short episodes of the $\sim \text{MeV}$ electron enhancements seem to be correlated to the energetic electron injections, the overall lower $\sim \text{MeV}$ electron fluxes in the geosynchronous orbit may be a consequence of the associated interplanetary phenomena (Fig. 1), as discussed below.

The radiation belt $\sim \text{MeV}$ electron flux decreases were reported during the impingement of the FF shocks on the magnetosphere (e.g., Hajra and Tsurutani, 2018b; Hajra et al., 2020). The assumed scenario is that the solar wind pressure pulses associated with interplanetary shocks cause the generation of coherent EMIC waves in the dayside magnetosphere (Remya et al., 2015; Tsurutani et al., 2016). Interestingly, the magnetic field spectrograms (Fig. 2h) show the EMIC wave generation coincident with the shock impingement. However, continuous generation of the EMIC waves during the substorms is facilitated by the continuous injection of energetic ($\sim 1 - 100 \text{ keV}$) protons as confirmed by the proton energy spectrograms (Fig. 2e). The EMIC waves can have parasitic resonant interaction with relativistic electrons, causing their pitch angle scattering and loss to the atmosphere (Thorne and Kennel, 1971; Meredith et al., 2003; Summers et al., 2007). There is another possibility for relativistic electron losses, that of “magnetopause shadowing” where the electrons gradient drift to the magnetopause and are lost into the solar wind (West et al., 1972; Li et al., 1997; Hudson et al., 2014). At this time, it is uncertain which of the two mechanisms dominates. It seems quite likely that both are occurring. It is possible that the dominant effect may vary from case to case.

3.2. Case study of SSSs during day 236 of year 2005

Fig. 3 shows another example of SSSs during day 236 (24 August) of year 2005, when the *Cluster 1* spacecraft was inside the magnetotail (Fig. 3a). The panels are in the same format as in Fig. 1. The SSSs occurred during the main phase of a super geomagnetic storm with the peak SYM-H of -179 nT at $\sim 11:50 \text{ UT}$ on day 236 (Fig. 3i).

Variations of the solar and interplanetary parameters indicate a complex interplanetary condition resulting from an interaction between two ICMEs and a corotating interaction region (CIR). According to the SOHO/LASCO

Table 2
Shock analysis.

Time (UT)	Type	Driver	Jump in interplanetary parameters					θ_{Bn} (°)	M_{ms}
			V_{sw} (km s ⁻¹)	N_{sw} (cm ⁻³)	P_{sw} (nPa)	T_{sw} (10 ⁵ K)	B_0 (nT)		
208/2004 22:48	FF	ICME	607–937	2.0–6.9	1.4–5.9	1.4–9.3	1.6–10.3	64	5.3
235/2005 20:24	FF	ICME	448–483	2.6–3.7	1.1–1.8	0.3–0.7	4.8–6.8	33	1.3
236/2005 06:14	FF	ICME	443–535	7.2–20.0	2.9–11.9	0.7–2.5	11.4–23.7	85	1.5
236/2005 20:53	FR	CIR	592–703	2.5–1.0	2.2–1.0	3.4–2.0	19.4–10.8	64	1.4

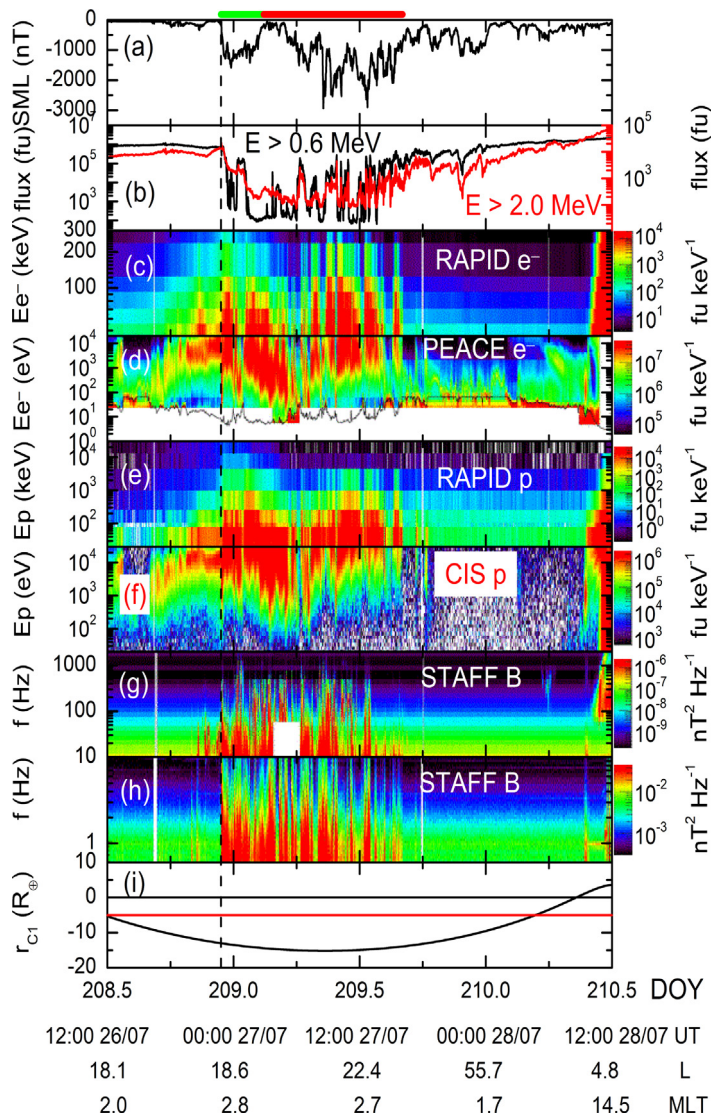


Fig. 2. Geosynchronous orbit and magnetotail plasma variations during the SSS events on day 209 of year 2004. From top to bottom, the panels are (a) the SML index (nT), (b) GOES 12 E1 > 0.6 MeV and E2 > 2.0 MeV electron fluxes (in flux unit/fu, 1 fu = cm⁻² s⁻¹ sr⁻¹) at the geosynchronous orbit, energy spectrograms (fu keV⁻¹) (c) of > 30 keV electrons, (d) of 0.6 eV to 26 keV electrons, (e) of > 30 keV protons, (f) of 5.0 eV to 32 keV protons, total B-field spectrograms (nT² Hz⁻¹) in (g) 10–2000 Hz range, and (h) 0.6–10 Hz range, and (i) Cluster 1 radial distance from Earth r_{C1} (R_E), respectively during days 208–210 of year 2004. Red horizontal line in panel (i) marks the SML < -2500 nT level. Vertical dashed black line marks the time of FF shock. Green and red horizontal bars at the top panel show the interplanetary sheath and MC, respectively. The magnetic local time (MLT) and the L-shell position of the spacecraft are mentioned at the bottom.

catalog, two halo CMEs erupted from the Sun at \sim 01:32 UT (speed \sim 1194 km s⁻¹) and at \sim 17:30 UT (speed \sim 2378 km s⁻¹) on day 234. In addition, the solar synoptic

map at 17:34 UT on day 234 provided by the Space Weather Prediction Center of National Oceanic and Atmospheric Administration (<https://www.swpc.noaa.gov/>)

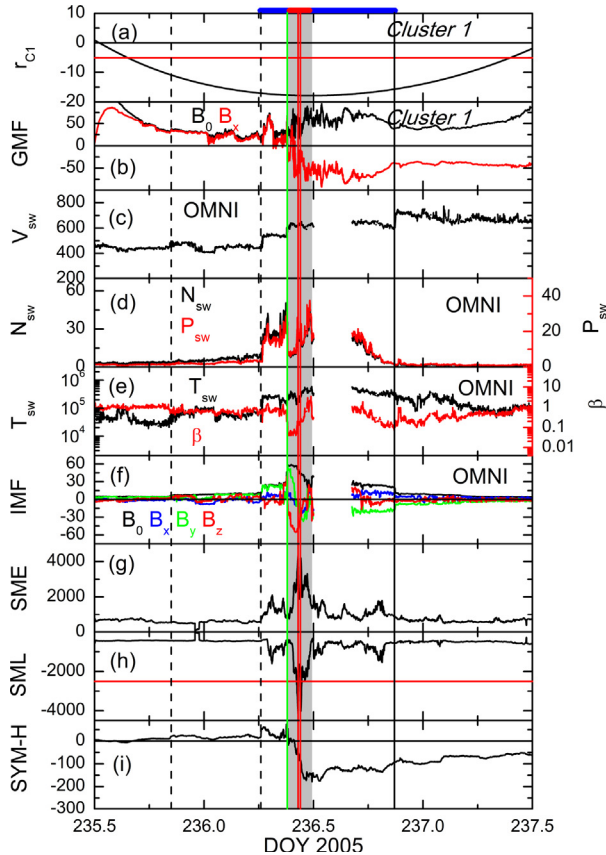


Fig. 3. Solar wind and interplanetary parameters during the SSS events on day 236 of year 2005. Panels are in the same format as in Fig. 1. Vertical lines indicate the times of the SSS SML peaks (red solid lines), fast forward shocks (black dashed lines), a fast reverse shock (black solid line) and a stream interface (green solid line). Blue bar on the top indicates the CIR interval. Shaded region and green bar on the top show an MC.

showed a coronal hole with negative polarity (i.e., magnetic field toward the Sun) around center of the Sun. A solar wind high-speed stream (HSS) emanated from this coronal hole was observed in the near-Earth solar wind measurements on days 236–237, ~2 days after the observation of the coronal hole. The peak HSS V_{sw} ($\sim 740 \text{ km s}^{-1}$) is consistent with an emanation from the coronal hole on day 234, and the sunward IMF direction (positive B_x and negative B_y values) during the HSS is consistent with the coronal hole polarity. Two FF shocks (shown by vertical dashed black lines) at $\sim 20:24 \text{ UT}$ on day 235 (FF_{235}), and at $\sim 06:14 \text{ UT}$ on day 236 (FF_{236}) seem to be associated with interplanetary counterparts of the CMEs. A stream interface (SI, vertical solid green line) observed at $\sim 09:07 \text{ UT}$ on day 236 (SI_{236}) was characterized by a sharp decrease in N_{sw} from ~ 32.4 to $\sim 11.5 \text{ cm}^{-3}$, accompanied by an abrupt increase in T_{sw} from $\sim 1.2 \times 10^5$ to $\sim 2.8 \times 10^5 \text{ K}$. V_{sw} exhibited an increase from ~ 529 to $\sim 605 \text{ km s}^{-1}$ across the SI. It separated a compressed, slow wind with a low alpha-to-proton density ratio from a compressed, fast wind with a higher ratio (not shown) (Belcher

and Davis, 1971; Burlaga, 1974; Hundhausen and Burlaga, 1975). The compressed solar wind plasma and IMF region is identified as a CIR (CIR_{236} , blue bar on the top). It extends from FF_{236} to a fast reverse (FR) shock (vertical solid black line) at $\sim 20:53 \text{ UT}$ on day 236 (FR_{236}). Interestingly, the region between $\sim 09:07 \text{ UT}$ and $\sim 11:43 \text{ UT}$ on day 236 is characterized by a low plasma- β , and smooth rotations in the IMF components. This represents an MC (MC_{236}).

The characteristic parameters of the shocks are listed in Table 2. FF_{235} caused an SI^+ of $\sim 10 \text{ nT}$ in SYM-H (Fig. 3i). However, it did not trigger any substorm. FF_{236} caused an SI^+ of $\sim 37 \text{ nT}$ and triggered a substorm with the SME and SML peaks of 2103 nT and -1605 nT , respectively at $\sim 07:27 \text{ UT}$ on day 236. No clear geomagnetic impact of FR_{236} was recorded.

Inside MC_{236} , IMF exhibited an abrupt southward turning at $\sim 09:09 \text{ UT}$, attained a peak southward component of -55.6 nT at $\sim 10:02 \text{ UT}$, and turned again to northward at $\sim 10:54 \text{ UT}$ on day 236. The IMF southward turning triggered a double-peak SSS at $\sim 09:41 \text{ UT}$. Two SML peaks of -4143 and -4017 nT are observed at $\sim 10:18$ and $\sim 10:37 \text{ UT}$, respectively (Table 1). The magnetotail GMF was significantly compressed (GMF $B_0 \sim 94.7 \text{ nT}$) and fluctuating during the MC_{236} – CIR_{236} interaction region (Fig. 3b). During the SSS peaks, the Cluster 1 spacecraft moved from the magnetic equator to the southern plasma sheet region, facilitating suitable exploration of the magnetotail plasma sheet.

Fig. 4 shows the plasma and wave activities in the tail region along with the $\sim \text{MeV}$ electron variation in the geosynchronous orbit during the SSS events on day 236 of year 2005. In the magnetotail region, plasma and wave activities during the SSSs are quite similar as were observed during the SSSs on day 209 of 2004 (Fig. 2). The SSSs are associated with flux enhancements of energetic electrons ($\sim 100 \text{ eV}$ – 100 keV , Fig. 4c–d) and protons (~ 1 – 300 keV , Fig. 4e–f). Isotropic distribution, from pitch angle 0° to 180° , of the energetic protons during the entire SSS interval (not shown) resulted in the generation of the EMIC waves (~ 0.1 – 5 Hz) as can be seen from the GMF spectrograms (Fig. 4h). Another origin of the observed EMIC waves is the creation of the waves in the dayside magnetopause by the shock impingements and transport of the same to the magnetotail. The EMIC waves caused pitch angle scattering and loss of the $\sim \text{MeV}$ electrons in the geosynchronous orbit (Fig. 4b).

Clearly, during both the SSS intervals (day 209 of 2004, and day 236 of 2005), magnetotail current sheet was largely turbulent by the injections of the energetic electrons and protons, and the resultant wave activity. The geosynchronous orbit exhibited loss of $\sim \text{MeV}$ electron fluxes during the SSSs. These consistent responses of the magnetotail, geosynchronous orbit and the auroral ionosphere were driven by the turbulent solar wind and interplanetary structures.

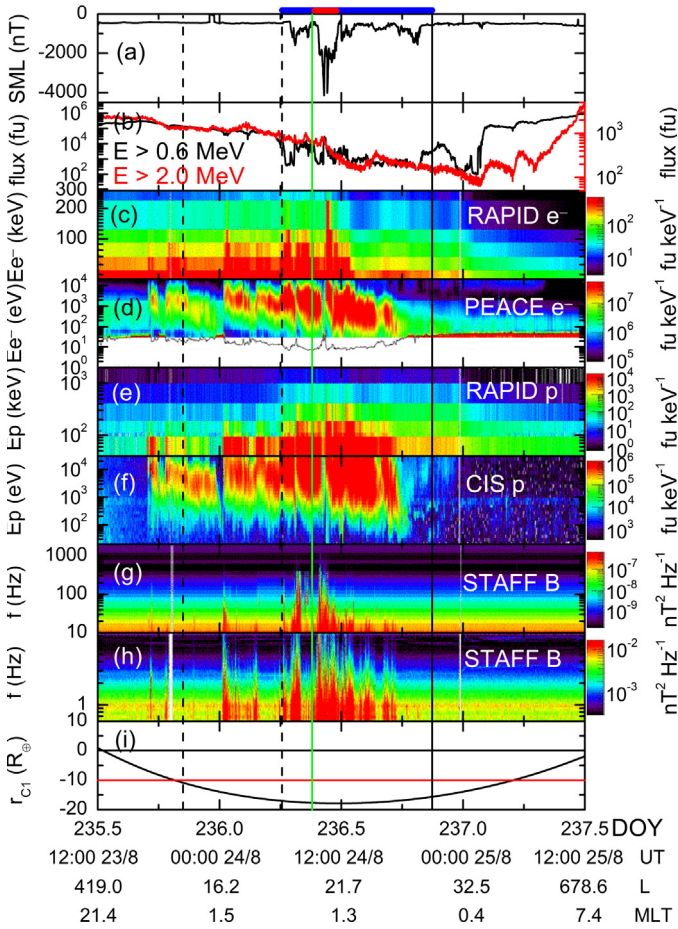


Fig. 4. Geosynchronous orbit and magnetotail plasma variations during the SSS events on day 236 of year 2005. Panels are in the same format as in Fig. 2. Vertical lines indicate the times of the fast forward shocks (black dashed lines), a fast reverse shock (black solid line), and a stream interface (green solid line). Blue and red bars on the top indicate the CIR and MC intervals.

3.3. Turbulence characteristics during the SSSs

Fig. 5 shows the Fourier power spectra of the IMF B_z , the magnetotail GMF B_x and the auroral SML index during the SSS events on day 209 of year 2004 (time series plots are repeated from Fig. 1). The spectral indices of the parameters are obtained by the power law fitting (shown by red line) with the power spectral density (PSD) variation. The spectral index is found to be significantly low for the IMF B_z (-1.85) compared to the GMF B_x (-2.17) and the SML index (-1.93).

Table 3 lists the spectral indices for the parameters during all SSSs under this present study. Suitable IMF B_z data are available for 3 of the 5 events studied. For all these 3 events, the IMF B_z exhibits the lowest spectral index (compared to GMF B_x and SML). Magnetotail GMF B_x and SML data are available for all 5 events. The GMF B_x has the highest spectral index in 3 cases and the SML index in 2 cases. The average spectral index (for all cases studied) is significantly low for the solar wind (-1.78 for IMF B_z with a standard deviation of $\sim 3\%$) compared to the mag-

netotail (-2.05 for GMF B_x with a standard deviation of $\sim 14\%$) and the auroral ionosphere (-2.02 for SML with a standard deviation of $\sim 8\%$). The spectral index gives the rate at which wave or turbulence power changes from low to high frequency region. Thus, the higher spectral indices in the magnetotail and auroral regions are indicative of the larger turbulence in those regions compared to the solar wind. Prior studies (e.g., Uritsky and Pudovkin, 1998) reported non-coincidence of the Fourier spectral forms of the solar wind parameters and the AE fluctuation spectra, indicating inner magnetospheric sources of the AE turbulence. Borovsky and Funsten (2003) studied the turbulence in the Earth's plasma sheet using the International Sun-Earth Explorer (ISEE) 2 plasma and magnetic field measurements. The plasma sheet turbulence was found to be a turbulence of eddies, rather than a turbulence of Alfvén waves or other MHD modes. Several studies (e.g., Antonova and Stepanova, 2021, and references therein) have demonstrated the importance of including reconnection phenomena observed inside the turbulent regions as a part of the turbulent tail dynamics. Vörös et al. (2006) explored the frequency dependence of the turbulence spectral index in the near-Earth plasma sheet and distant tail. The spectral index was suggested to vary between -0.5 and -1.5 for frequencies less than 0.01 Hz , while it varies between -1.7 and -3.0 for higher frequencies. The magnetotail GMF B_x and SML spectral indices obtained in the present work (Table 3) are consistent with these results. Uncertainty in the values shown in Table 3 may be associated with the large amplitudes of coherent structures and the low frequencies found in the plasma sheet, as mentioned by Borovsky and Funsten (2003). The solar wind turbulence is significantly amplified after crossing the bow shock, and plasma flows are generated in the magnetosheath region. In the nightside, eddy vortices are generated due to those large-scale magnetospheric flows, which can drive the tail turbulence (Antonova and Stepanova, 2021). Further, the geomagnetic indices are generally correlated to the upstream solar wind turbulence, and thus, as the amplitude of solar wind turbulence increases, the geomagnetic activity increases as well (D'Amicis et al., 2020). The geomagnetic activity can also be intensified by inner processes and due to the presence of the magnetospheric boundaries. In addition, the higher turbulence may be associated with the tail reconnection and substorm triggering, and energetic particle injection, leading to the SSSs, reflected in intense and fluctuating SML variation. The highly turbulent magnetotail is conducive to plasma instability and generation of electromagnetic plasma waves observed in Figs. 2 and 4.

3.4. Periodic variations during the SSS events: wavelet and cross-wavelet analyses

From the Fourier power spectra analysis (Fig. 5, Table 3), it can be seen that the power decreases with increase of frequency. However, there are oscillations in the time

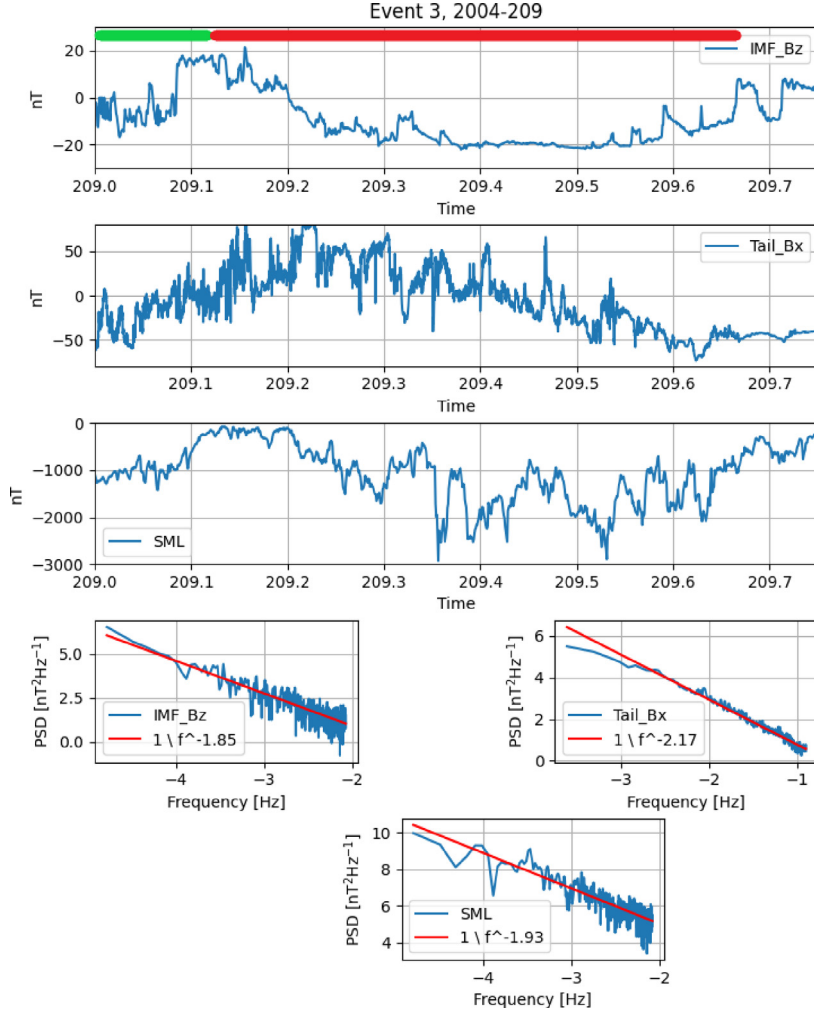


Fig. 5. Fourier power spectra of IMF B_z , GMF B_x , and SML for the SSS events on day 209 of year 2004. In each plot, the red line indicates the power-law fitting of the power spectral density (PSD). Green and red horizontal bars at the top panel show the interplanetary sheath and MC, respectively.

Table 3
Spectral indices of IMF B_z , GMF B_x and SML obtained from Fourier spectral analysis during the SSS events.

Event	IMF B_z	GMF B_x	SML
2001_310	–	–1.80	–2.25
2003_302	–	–1.72	–2.05
2004_209	–1.85	–2.17	–1.93
2004_313	–1.73	–2.36	–1.80
2005_236	–1.77	–2.20	–2.05
Mean ± STD ¹	-1.78 ± 0.06	-2.05 ± 0.28	-2.02 ± 0.17

¹ STD stands for standard deviation from the mean.

series and in the spectrum, which can be unsteady. We now apply the WT analysis to identify any periodicity in the solar wind, magnetosphere and ionosphere, as well as where or when it occurs. In addition, the XWT analysis is applied to determine the periods at which the magnetosphere responds to the solar wind forcing. The WT and XWT analysis results for the SSSs on day 209 of year 2004 are shown in Fig. 6, Fig. 7, respectively. Similar analyses are performed for all SSS events in this work, and the

results are summarized in Table 4 (WT) and Table 5 (XWT). The WT/XWT periodicity has been classified as local (L) if a signal has enhanced power only during a small interval, as intermittent (I) if the signal appears over longer interval but intermittently. For the continuous (C) and quasi-continuous (QC) periodicities, the signal is enhanced for the entire interval or most of the interval, respectively (Souza et al., 2016).

From the IMF B_z wavelet spectrum shown in Fig. 6a, a strong power can be seen centered around the ~2.5-hour period inside the “cone of influence”. As the “edge effect” may be significant outside the cone of influence, any period observed outside this region is ignored. The wavelet spectrum shows an intermittent (I) energy distribution around the 2.5-h period, where high energy density is observed during two intervals, days $\sim 209 - 209.4$, and days $\sim 209.55 - 209.75$. This period is in the range of substorm periodicity (~2–3 hours) during fluctuating IMF B_z (Huang et al., 2003; Huang et al., 2004). Two additional periods with lower energy are also observed in the global wavelet spectrum, ~ 1.0 and ~ 0.6 hours (Fig. 6b, Table

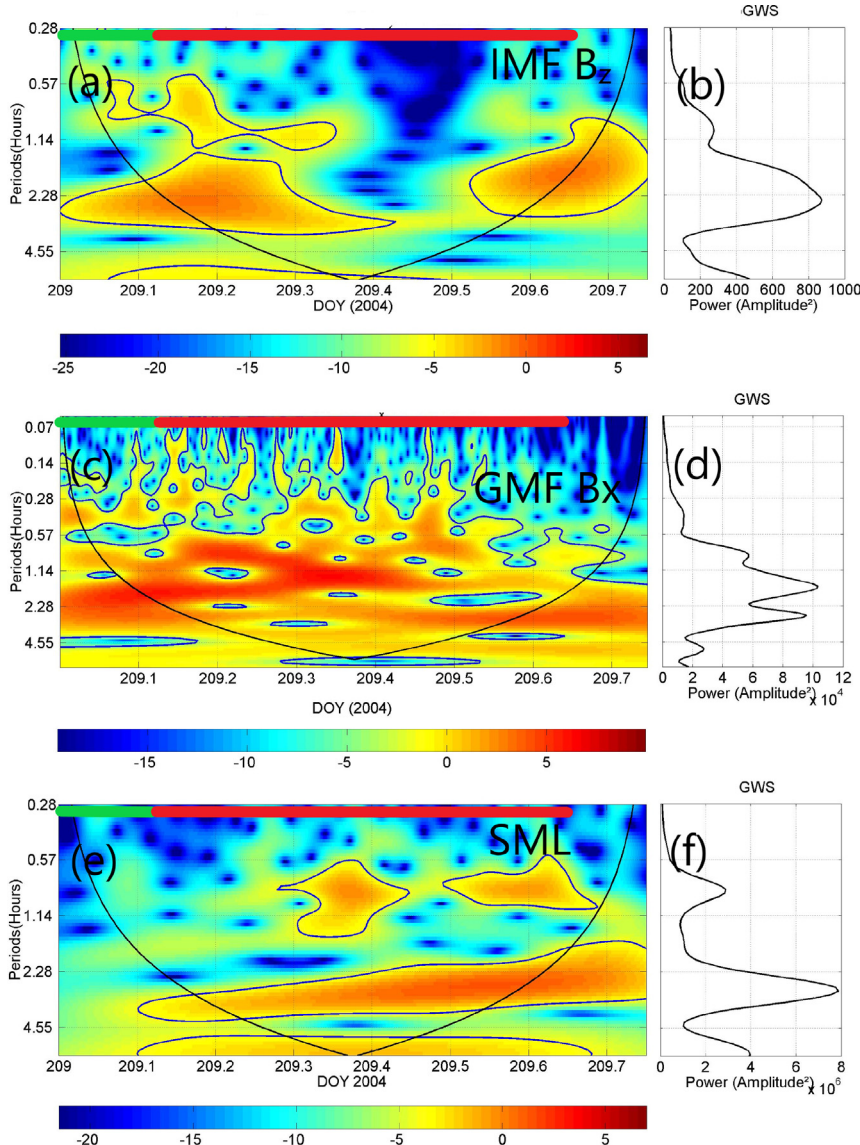


Fig. 6. Wavelet analysis of the IMF B_z , magnetotail GMF B_x and the auroral SML index during the SSS events on day 209 of year 2004. The left panels show the wavelet spectrum periodograms. The cone of influence is shown by the black curve in the wavelet panels. The color bars below the panels indicate the wavelet spectral power of the observed periods in arbitrary units. Panels on the right show the global wavelet spectrum indicating the significant periods. Green and red horizontal bars at top of the left panels show the interplanetary sheath and MC, respectively.

4). It can be noted that the high-frequency IMF B_z fluctuations are seen near the sheath region (shown by green horizontal bar at the top) and at the beginning of the MC (red horizontal bar at the top), where B_z is more fluctuating. The period without fluctuations in the wavelet spectrum corresponds to the MC interval where B_z is smooth.

The magnetotail GMF B_x wavelet (Fig. 6c) is found to be characterized by more smaller-scale activity during the SSSs. From the corresponding global wavelet spectrum (Fig. 6d), ~ 1.6 -hour period has the strongest amplitude, followed by the amplitudes of ~ 2.7 , ~ 0.9 , ~ 5.2 , and ~ 0.4 hour periods (in the decreasing order of amplitude) (Table 4). The ~ 1.6 and ~ 5.2 hour periods have the quasi-continuous (QC) distributions in time (from day ~ 209 to ~ 209.65 , and from ~ 209.18 to ~ 209.75 , respectively), and ~ 2.7 -hour has a continuous (C) distribution

during entire interval of the SSSs. On the other hand, the periods of ~ 0.4 and ~ 0.9 hours show intermittent (I) distributions. For example, the regions of higher energy for the ~ 0.4 hour period are around days 209.05, 209.10, 209.30, 209.40, and 209.50. It can be noted that these correspond to the periods where we observed high-frequency oscillations in the IMF B_z wavelet spectrum (Fig. 6a). Huang et al. (2003) suggested that a magnetospheric resonant state may be excited when comparable periods of solar wind pressure and the substorm cycle time occur. As we found a periodicity of 2.5 hours in the IMF B_z , the ~ 5.2 hour period may be a harmonic of the 2.7 hour periodicity identified in the GMF B_x component.

The global wavelet spectrum of the SML index (Fig. 6f) clearly shows two significant periods of ~ 2.9 and ~ 0.8 hours (in the decreasing order of amplitude). From

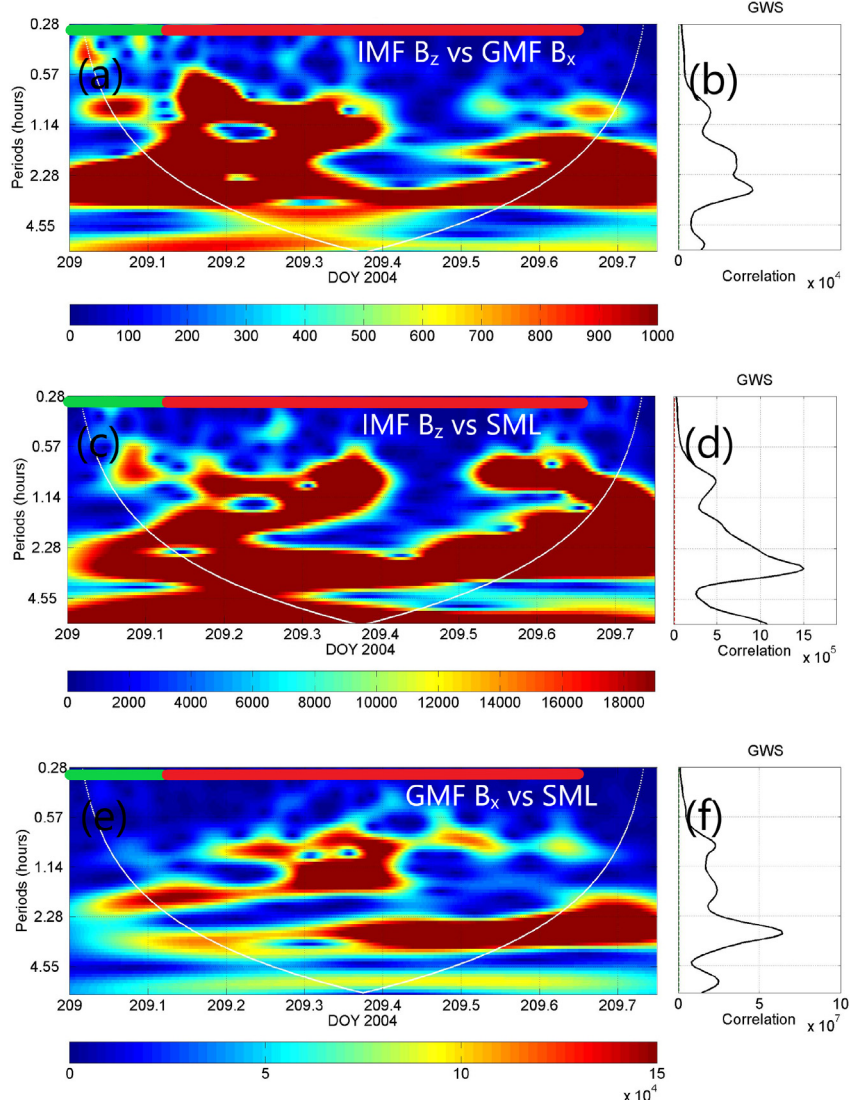


Fig. 7. Cross-wavelet analysis of IMF B_z and magnetotail GMF B_x , IMF B_z and SML index, and GMF B_x and SML index during the SSS events on day 209 of year 2004. The left panels show the cross-wavelet spectrum periodograms. The cone of influence is shown by the white curve in the cross-wavelet panels. The color bars below the panels indicate the cross-wavelet spectral power of the observed periods in arbitrary units. Panels on the right show the global wavelet spectrum indicating the significant common periods. Green and red horizontal bars at top of the left panels show the interplanetary sheath and MC, respectively.

Table 4

Wavelet analysis. Dominant periods (in hours) after remove long-term trend (in the decreasing order of amplitude). QC indicates quasi-continuous, I indicates intermittent, C indicates continuous, and L indicates Local distributions.

Event	IMF B_z	GMF B_x	SML
2001_310	–	2.1 ^{QC} , 0.5 ^I	2.6 ^{QC} , 1.3 ^L , 0.7 ^I
2003_302	–	3.0 ^{QC} , 1.8 ^{QC} , 1.0 ^I , 0.6 ^I , 0.5 ^I	2.5 ^{QC} , 3.9 ^{QC} , 1.4 ^L , 0.8 ^L
2004_209	2.5 ^I , 1.0 ^I , 0.6 ^I	1.6 ^{QC} , 2.7 ^C , 0.9 ^I , 5.2 ^{QC} , 0.4 ^I	2.9 ^{QC} , 0.8 ^I
2004_313	1.2 ^{QC} , 1.7 ^L , 2.9 ^{QC}	1.7 ^L , 1.2 ^L	2.3 ^{QC} , 3.3 ^C , 1.5 ^L , 0.9 ^L
2005_236	0.8 ^L , 0.5 ^I , 1.8 ^{QC}	2.3 ^C , 1.2 ^L , 0.6 ^I	1.4 ^L , 2.5 ^L , 0.4 ^L , 0.7 ^L

the wavelet spectrum (Fig. 6e), the ~ 2.9 hours period has a quasi-continuous (QC) distribution (between day ~ 209.1 and 209.75), while ~ 0.8 has an intermittent (I) distribution, where the two regions with higher energy are noted during the SSS peaks, around days 209.35 and 209.60. One can notice that the intermittent (I) distribution

observed around 1.0 hour is found in the three parameters/regions, IMF B_z (1.0 hour), magnetotail GMF B_x (0.9 hour) and the SML index (0.8 hour).

From Table 4 it can be noted that the intermittent (I) energy distributions ($\sim 45\%$) dominate the IMF B_z periodicities, followed by the quasi-continuous (QC, $\sim 33\%$) and

Table 5

Cross-wavelet analysis. Dominant periods in hour (in the decreasing order of amplitude).

Event	IMF B_z –GMF B_x	IMF B_z –SML	GMF B_x –SML
2001_310	—	—	3.5 ^{QC} , 1.5 ^L , 0.6 ^I
2003_302	—	—	2.4 ^L , 3.4 ^{QC} , 1.0 ^L
2004_209	2.8 ^C , 1.8 ^I , 1.0 ^I	3.0 ^C , 0.9 ^I	2.9 ^{QC} , 5.7 ^{QC} , 1.6 ^I , 0.9 ^I
2004_313	1.2 ^L , 1.7 ^L , 2.9 ^L	3.2 ^L , 2.0 ^L , 1.3 ^L	2.2 ^{QC} , 1.3 ^L , 3.5 ^L
2005_236	2.1 ^L , 0.9 ^L , 0.6 ^L	1.6 ^L , 0.8 ^L , 0.4 ^L	2.5 ^{QC} , 1.3 ^L

local (L, $\sim 22\%$) distributions. In the magnetotail GMF B_x , periodicities ≤ 1.0 hour show intermittent (I) variation, while the periodicities between ~ 1 and 1.5 hours are local (L), and periodicities > 1.5 hours are continuous (C) or quasi-continuous (QC) in the energy distribution. In the auroral ionospheric SML, periodicities > 1.5 hours have mainly the continuous (C) and quasi-continuous (QC) distributions. Below ~ 1.5 hours, the periodicities are intermittent (I) or local (L) in energy distribution. In summary, the inner magnetosphere (GMF B_x) and ionosphere (SML) seem to respond quasi-periodically at $\sim 1.5 - 4$ hours, and sporadically at shorter timescales of $\sim 0.5 - 1.5$ hours. In the magnetosphere, the highest amplitudes are found for the $\sim 2 - 4$ hours periodicities.

From the global XWT spectrum between the IMF B_z and magnetotail GMF B_x (Fig. 7b), three periods of high correlation can be observed. The most intense correlation, observed around 2.8-h, exhibits a continuous (C) distribution during the entire interval of the SSSs (Fig. 7a). The other two periods with high correlation, ~ 1.8 -hours and ~ 1.0 -hours, exhibit intermittent (I) distributions. For the period around 1.8-h, two large regions are seen in the XWT spectrum, the first from day ~ 209.11 to ~ 209.30 , and the second from day ~ 209.50 to the end of the interval. At least three regions of higher correlation can be observed from the XWT spectrum for the ~ 1.0 -hour period: between day 209.04 and 209.10, between day 209.15 and 209.39, and between day 209.65 and 209.70. A fourth region, not so intense, from day 209.51 to 209.57, is also noticed.

From the XWT analysis between the IMF B_z and SML index (Fig. 7d), two high correlation periods are ~ 3.0 hours and ~ 1.0 hour. The ~ 3.0 -hour period has a continuous (C) distribution. On the other hand, the ~ 1.0 hour period exhibits an intermittent (I) distribution, with high correlations around days $\sim 209.06 - 209.12$, $\sim 209.16 - 209.29$, $\sim 209.32 - 209.41$, and $\sim 209.52 - 209.67$ (Fig. 7c). Interestingly, the IMF B_z –SML XWT spectrum is almost identical to the IMF B_z –GMF B_x XWT spectrum (Fig. 7a).

The XWT analysis between the magnetotail GMF B_x and SML (Fig. 7f) shows the highest correlation for a period of ~ 2.8 hours. The quasi-continuous (QC) distribution of this period can be observed from day ~ 209.16 up to the end of the interval (Fig. 7e). The ~ 1.6 hours and ~ 0.9 hour periods exhibit intermittent (I) distributions, with high correlation regions around days $\sim 209.05 - 209.20$ and $\sim 209.27 - 209.43$ for the period

~ 1.6 hours, and around days 209.20–209.30, 209.31–209.43, 209.47–209.54 and 209.60–209.66 for the period ~ 0.9 hour.

In the XWT spectra shown in Fig. 7, the low correlation period for high-frequency ~ 1 hour oscillations correspond to the smooth part of the MC (red horizontal bar), where there are no IMF B_z fluctuations at this scale, and therefore no modulating effect on the magnetosphere. However, there is continuous energy injection from the solar wind due to southward IMF B_z and this may be reflected in the high correlation values persistent across this interval for periods longer than ~ 2 hours.

From Table 5 it can be observed that local (L) distribution dominates most of the periods, particularly in the XWTs between the IMF B_z and the GMF B_x , and between the IMF B_z and the SML index. Similar results were found by Franco et al. (2019) studying the magnetotail response to solar wind fluctuations during high-intensity long-duration continuous AE activity (HILDCAA) events (Tsurutani and Gonzalez, 1987; Hajra et al., 2013), where local (L) distribution was dominant in the XWT analysis between IMF B_z and magnetotail GMF B_x . In the XWT spectrum between the magnetotail GMF B_x and the SML index, the quasi-continuous (QC) distribution dominates large periods ($\sim 2 - 5$ hours), while the local (L) and intermittent (I) behaviors are observed for the shorter periods (< 2 hours).

Overall, the solar wind-magnetosphere coupling during the SSSs is a continuous injection of energy from the solar wind to the magnetosphere, which is highly modulated by high-frequency intermittent oscillations in the IMF B_z . These periods are more sporadic for periodicities shorter than ~ 2 hours and quasi-continuous for periodicities between ~ 2 and ~ 4 hours. Magnetosphere and auroral region respond to both scales. During substorms, it is known that the magnetosphere can have direct forcing from the solar wind or internal oscillations due to energy injection (e.g., Akasofu, 1964; Akasofu, 1981; Tsurutani and Meng, 1972; Rostoker et al., 1980; Borovsky et al., 1993). Both mechanisms seem to be occurring during the SSSs.

4. Summary and conclusions

We studied the inner magnetotail variability during SSSs for the first time. During the SSSs driven by interplanetary MCs, plasma turbulence is found to evolve and intensify from the solar wind to the inner magnetotail and iono-

sphere. Fourier spectral analysis and wavelet analysis indicate a clear increase in turbulence from the solar wind to the magnetotail and auroral ionosphere during the SSSs. This is associated with the EMIC wave activity resulting from the shock compression of the magnetosphere, and the temperature anisotropy of the injected energetic protons. An important consequence of the SSS EMIC wave activity is a significant loss of the \sim MeV electrons through the pitch angle scattering.

In a recent study (Tsurutani and Hajra, 2021), it was observed that the SSSs are the most effective geomagnetic event in causing the strongest geomagnetically induced currents (GICs) at the subauroral region. The intense, low-frequency (~ 0.001 – 1 Hz) currents are known to flow in ground-based long conducting systems owing to rapid changes of the geomagnetic fields ($\text{dB}/\text{dt} > 1 \text{nT s}^{-1}$) (Campbell, 1980; Akasofu and Aspnes, 1982; Lakhina et al., 2021; Hajra, 2022a,b, and references therein). Turbulent and intense auroral activity during the SSSs seem to efficiently lead to the dB/dt changes.

During these “extreme” substorms, the magnetosphere is in a much more disturbed state than during nominal substorms. For instance, Echer et al. (2017) have studied the magnetospheric response, including magnetotail, during HSS-driven storms and substorms. It was found that the magnetosphere exhibits a periodic response from 1.8 to 3 hours to solar wind HSS fluctuations. These responses were found to be globally consistent in the magnetotail, geosynchronous orbit, auroral region and ground-based magnetometers. However, during the SSS events (present work), the shock compression of the magnetosphere, and reconnection between IMF and geomagnetic fields are significantly stronger. During the SSSs, the solar wind-magnetosphere coupling seems to occur at some preferred periods of ~ 2 –3 hours, close to those observed for ordinary substorms (e.g. Echer et al., 2017). However, the periodicities during the SSSs are found to be less continuous and more intermittent than during the nominal substorms. This behaviour probably resulted from the nature of solar wind coupling during the SSSs, namely the strong magnetic compression followed by long-period reconnection between the MC fields and the dayside magnetopause fields.

5. Final comments

The term “supersubstorms” or SSSs was first introduced by Tsurutani et al. (2015) for the substorms with the SML intensities $< -2500 \text{nT}$. Two important questions are: why was the SML threshold chosen to be -2500nT ? And what is difference between SSSs and nominal substorms?

To answer the first question, the SML minimum value of -2500nT was “arbitrarily” chosen “to examine extremely intense substorms” (Tsurutani et al., 2015). How extreme are they? Tanskanen (2009), from a statistical study of ~ 6000 substorms occurring between 1993 and 2003, reported an average substorm strength of

$\sim -396 \pm 54 \text{nT}$. An average substorm intensity of $\sim -405 \pm 48 \text{nT}$ was suggested from another analysis of 8717 substorms identified from 1993 to 2008 by Tanskanen et al. (2011). Thus, the SSS SML threshold (-2500nT) is significantly high compared to an “ordinary” substorm. However, what happens for events with higher SML thresholds like -2000nT or so? This could be verified in a future work.

The second question can be discussed in the light of previous and present works. Hajra and Tsurutani (2018a) showed that the SSSs have a different auroral evolution than a nominal substorm. In contrast to the standard midnight sector substorm onset and following expansion, SSSs were shown to exhibit intense pre-midnight and post-midnight auroras, with the midnight sector devoid of auroras. Precursor energy input through magnetic reconnection was found to be insufficient to balance the large ionospheric energy dissipation during the SSSs. This is another contrasting feature of SSSs compared to nominal substorms. Observed magnetospheric turbulence during the SSS events (present work) is not much different than the magnetospheric turbulence during nominal substorms. How does the SSS SML turbulence compare with the SML turbulence during nominal substorms? Or how is the dependence of turbulence on the substorm SML strength, if any? This is not known yet. A future comparative study involving SSS and nominal substorm turbulence could be interesting.

Declaration of Competing Interest

The authors declare that they have no known competing financial interests or personal relationships that could have appeared to influence the work reported in this paper.

Acknowledgments

The work of R. Hajra is funded by the Science and Engineering Research Board (SERB, Grant No. SB/S2/RJN-080/2018), a statutory body of the Department of Science and Technology (DST), Government of India through the Ramanujan Fellowship. The work at the University of Science and Technology of China is funded by the Chinese Academy of Sciences “Hundred Talents Program”. E. Echer would like to thank Brazilian agencies for research grants: CNPq (contract No. PQ-302583/2015-7, PQ-301883/2019-0) and FAPESP (2018/21657-1). The work of A. M. S. Franco is funded by the Brazilian CNPq agency (project No. PQ-300969/2020-1, PQ-301542/2021-0, PQ-300160/2021-6). The work of M. J. A. Bolzan is supported by CNPq agency (contract No. PQ-302330/2015-1, PQ-305692/2018-6) and FAPEG agency (contract No. 2012.1026.7000905). We would like to thank the reviewers for extremely valuable suggestions that substantially improved the manuscript.

References

- Abraham-Shrauner, B., Yun, S.H., 1976. Interplanetary shocks seen by Ames Plasma Probe on Pioneer 6 and 7. *J. Geophys. Res.* 81, 2097–2102. <https://doi.org/10.1029/JA081i013p02097>.
- Akasofu, S.I., 1964. The development of the auroral substorm. *Planet. Space Sci.* 12, 273–282. [https://doi.org/10.1016/0032-0633\(64\)90151-5](https://doi.org/10.1016/0032-0633(64)90151-5).
- Akasofu, S.I., 1981. Energy coupling between the solar wind and the magnetosphere. *Space Sci. Rev.* 28, 121–190. <https://doi.org/10.1007/BF00218810>.
- Akasofu, S.I., Aspnes, J.D., 1982. Auroral effects on power transmission line systems. *Nature* 295, 136–137. <https://doi.org/10.1038/295136a0>.
- Akasofu, S.I., Chao, J., 1980. Interplanetary shock waves and magnetospheric substorms. *Planet. Space Sci.* 28, 381–385. [https://doi.org/10.1016/0032-0633\(80\)90042-2](https://doi.org/10.1016/0032-0633(80)90042-2).
- Antonova, E.E., Stepanova, M.V., 2021. The impact of turbulence on physics of the geomagnetic tail. *Front. Astron. Space Sci.* 8, 622570. <https://doi.org/10.3389/fspas.2021.622570>.
- Artamonov, A.A., Mishev, A.L., Usoskin, I.G., 2016. Atmospheric ionization induced by precipitating electrons: Comparison of CRAC: EPII model with a parametrization model. *J. Atmos. Solar Terr. Phys.* 149, 161–166. <https://doi.org/10.1016/j.jastp.2016.04.020>.
- Bailey, D.H., Swarztrauber, P.N., 1994. A fast method for the numerical evaluation of continuous Fourier and Laplace transforms. *SIAM J. Sci. Comp.* 15, 1105–1110. <https://doi.org/10.1137/0915067>.
- Baker, D.N., Pulkkinen, T.I., Angelopoulos, V., Baumjohann, W., McPherron, R.L., 1996. Neutral line model of substorms: Past results and present view. *J. Geophys. Res.* 101, 12975–13010. <https://doi.org/10.1029/95JA03753>.
- Balogh, A., Dunlop, M.W., Cowley, S.W.H., Southwood, D.J., Thomsen, J.G., Glassmeier, K.H., Musmann, G., LÜHR, H., Buchert, S., AcuNA, M.H., Fairfield, D.H., Slavin, J.A., Riedler, W., Schwinschuh, K., Kivelson, M.G., 1997. The Cluster magnetic field investigation. *Space Sci. Rev.* 79, 65–91. <https://doi.org/10.1023/A:1004970907748>.
- Belcher, J.W., Davis Jr., L., 1971. Large-amplitude Alfvén waves in the interplanetary medium, 2. *J. Geophys. Res.* 76, 3534–3563. <https://doi.org/10.1029/JA076i016p03534>.
- Bolzan, M., Rosa, R., 2012. Multifractal analysis of interplanetary magnetic field obtained during CME events. *Ann. Geophys.* 30, 1107–1112. <https://doi.org/10.5194/angeo-30-1107-2012>.
- Borovsky, J.E., Funsten, H.O., 2003. MHD turbulence in the Earth's plasma sheet: Dynamics, dissipation, and driving. *J. Geophys. Res.* 108, 284. <https://doi.org/10.1029/2002JA009625>.
- Borovsky, J.E., Nemzek, R.J., Belian, R.D., 1993. The occurrence rate of magnetospheric-substorm onsets: Random and periodic substorms. *J. Geophys. Res.* 98, 3807–3813. <https://doi.org/10.1029/92JA02556>.
- Bracewell, R.N., 2014. *The Fourier Transform and Its Applications*, 3rd ed. CBS Publishers & Distributors Pvt. Ltd..
- Burlaga, L., Sittler, E., Mariani, F., Schwenn, R., 1981. Magnetic loop behind an interplanetary shock: Voyager, Helios, and IMP 8 observations. *J. Geophys. Res.* 86, 6673–6684. <https://doi.org/10.1029/JA086iA08p06673>.
- Burlaga, L.F., 1974. Interplanetary stream interfaces. *J. Geophys. Res.* 79, 3717–3725. <https://doi.org/10.1029/JA079i025p03717>.
- Campbell, W.H., 1980. Observation of electric currents in the Alaska oil pipeline resulting from auroral electrojet current sources. *Geophys. J. Int.* 61, 437–449. <https://doi.org/10.1111/j.1365-246X.1980.tb04325.x>.
- Carlson, C.W., Pfaff, R.F., Watzin, J.G., 1998. The fast auroral snapshot (FAST) mission. *Geophys. Res. Lett.* 25, 2013–2016. <https://doi.org/10.1029/98GL01592>.
- Cornilleau-Wehrlin, N., Chauveau, P., Louis, S., Meyer, A., Nappa, J.M., Perraut, S., Rezeau, L., Robert, P., Roux, A., De Villedary, C., De Conchy, Y., Friel, L., Harvey, C.C., Hubert, D., Lacombe, C., Manning, R., Wouters, F., Lefevre, F., Parrot, M., Pinçon, J.L., Poirier, B., Kofman, W., Louarn, P., 1997. The Cluster spatio-temporal analysis of field fluctuations (STAFF) experiment. *Space Sci. Rev.* 79, 107–136. <https://doi.org/10.1023/A:1004979209565>.
- Cornwall, J.M., 1965. Cyclotron instabilities and electromagnetic emission in the ultra low frequency and very low frequency ranges. *J. Geophys. Res.* 70, 61–69. <https://doi.org/10.1029/JZ070i001p00061>.
- D'Amicis, R., Telloni, D., Bruno, R., 2020. The effect of solar-wind turbulence on magnetospheric activity. *Front. Phys.* 8, 604857. <https://doi.org/10.3389/fphy.2020.604857>.
- Despirak, I.V., Lyubchich, A.A., Kleimenova, N.G., 2019. Supersubstorms and conditions in the solar wind. *Geomag. Aeron.* 59, 170–176. <https://doi.org/10.1134/S0016793219020075>.
- Dungey, J.W., 1961. Interplanetary magnetic field and the auroral zones. *Phys. Rev. Lett.* 6, 47–48. <https://doi.org/10.1103/PhysRevLett.6.47>.
- Echer, E., Korth, A., Bolzan, M.J.A., Friedel, R.H.W., 2017. Global geomagnetic responses to the IMF B_z fluctuations during the September/October 2003 high-speed stream intervals. *Ann. Geophys.* 35, 853–868. <https://doi.org/10.5194/angeo-35-853-2017>.
- Escoubet, C.P., Schmidt, R., Goldstein, M.L., 1997. Cluster – science and mission overview. *Space Sci. Rev.* 79, 11–32. <https://doi.org/10.1023/A:1004923124586>.
- Fang, X., Randall, C.E., Lummerzheim, D., Wang, W., Lu, G., Solomon, S.C., Frahm, R.A., 2010. Parameterization of monoenergetic electron impact ionization. *Geophys. Res. Lett.* 37, L22106. <https://doi.org/10.1029/2010GL045406>.
- Franco, A.M.S., Echer, E., Bolzan, M.J.A., 2019. Wavelet analysis of the magnetotail response to solar wind fluctuations during HILDCAA events. *Ann. Geophys.* 37, 919–929. <https://doi.org/10.5194/angeo-37-919-2019>.
- Gjerloev, J.W., 2009. A global ground-based magnetometer initiative. *Eos Trans. AGU* 90, 230–231. <https://doi.org/10.1029/2009EO270002>.
- Gjerloev, J.W., 2012. The SuperMAG data processing technique. *J. Geophys. Res.* 117, A09213. <https://doi.org/10.1029/2012JA017683>.
- Gonzalez, W.D., Joselyn, J.A., Kamide, Y., Kroehl, H.W., Rostoker, G., Tsurutani, B.T., Vasyliunas, V.M., 1994. What is a geomagnetic storm?. *J. Geophys. Res.* 99, 5771–5792. <https://doi.org/10.1029/93JA02867>.
- Hajra, R., 2002a. Intense Geomagnetically Induced Currents (GICs): Association with Solar and Geomagnetic Activities. *Solar Phys.* 297, 14. <https://doi.org/10.1007/s11207-021-01945-8>.
- Hajra, R., 2022b. Intense, long-duration geomagnetically induced currents (GICs) caused by intense substorm clusters. *Space Weather* 20. <https://doi.org/10.1029/2021SW002937>.
- Hajra, R., Echer, E., Tsurutani, B.T., Gonzalez, 2013. Solar cycle dependence of High-Intensity Long-Duration Continuous AE Activity (HILDCAA) events, relativistic electron predictors?. *J. Geophys. Res. Space Physics* 118, 5626–5638. <https://doi.org/10.1002/jgra.50530>.
- Hajra, R., Franco, A.M.S., Echer, E., Bolzan, M.J.A., 2021. Long-term variations of the geomagnetic activity: a comparison between the strong and weak solar activity cycles and implications for the space climate. *J. Geophys. Res.* 126, e2020JA028695. <https://doi.org/10.1029/2020JA028695>.
- Hajra, R., Tsurutani, B.T., 2018a. Interplanetary shocks inducing magnetospheric supersubstorms ($SML < -2500$ nT): Unusual auroral morphologies and energy flow. *Astrophys. J.* 858, 123. <https://doi.org/10.3847/1538-4357/abaed>.
- Hajra, R., Tsurutani, B.T., 2018b. Chapter 14 - Magnetospheric killer relativistic electron dropouts (REDs) and repopulation: A cyclical process. In: Buzulukova, N. (Ed.), *Extreme Events in Geospace*. Elsevier, pp. 373–400. <https://doi.org/10.1016/B978-0-12-812700-1.00014-5>.
- Hajra, R., Tsurutani, B.T., Echer, E., Gonzalez, W.D., Gjerloev, J.W., 2016. Supersubstorms ($SML < -2500$ nT): Magnetic storm and solar cycle dependences. *J. Geophys. Res.* 121, 7805–7816. <https://doi.org/10.1002/2015JA021835>.
- Hajra, R., Tsurutani, B.T., Lakhina, G.S., 2020. The complex space weather events of 2017 September. *Astrophys. J.* 899, 3. <https://doi.org/10.3847/1538-4357/aba2c5>.

- Hayakawa, M., Ohmi, N., Parrot, M., Lefevre, F., 1986. Direction finding of ELF hiss emissions in a detached plasma region of the magnetosphere. *J. Geophys. Res.* 91, 135–141. <https://doi.org/10.1029/JA091iA01p00135>.
- Huang, C.S., Le, G., Reeves, G.D., 2004. Periodic magnetospheric substorms during fluctuating interplanetary magnetic field B_z . *Geophys. Res. Lett.* 31, L14801. <https://doi.org/10.1029/2004GL020180>.
- Huang, C.S., Reeves, G.D., Borovsky, J.E., Skoug, R.M., Pu, Z.Y., Le, G., 2003. Periodic magnetospheric substorms and their relationship with solar wind variations. *J. Geophys. Res.* 108, 1255. <https://doi.org/10.1029/2002JA009704>.
- Hudson, M.K., Baker, D.N., Goldstein, J., Kress, B.T., Paral, J., Toffoletto, F.R., Wiltberger, M., 2014. Simulated magnetopause losses and Van Allen Probe flux dropouts. *Geophys. Res. Lett.* 41, 1113–1118. <https://doi.org/10.1002/2014GL059222>.
- Hugoniot, H., 1887. Mémoire sur la propagation des mouvements dans les corps et spécialement dans les gaz parfaits (première partie). *J. de l'École Polytech.* 57, 3–97.
- Hugoniot, H., 1889. Mémoire sur la propagation des mouvements dans les corps et spécialement dans les gaz parfaits (deuxième partie). *J. de l'École Polytech.* 58, 1–125.
- Hundhausen, A.J., Burlaga, L.F., 1975. A model for the origin of solar wind stream interfaces. *J. Geophys. Res.* 80, 1845–1848. <https://doi.org/10.1029/JA080i013p01845>.
- Iyemori, T., Takeda, M., Nose, M., Odagi, Y., Toh, H., 2010. Mid-latitude Geomagnetic Indices ASY and SYM for 2009 (Provisional). Internal Report of Data Analysis Center for Geomagnetism and Space Magnetism (Japan: Kyoto University). URL: <http://wdc.kugi.kyoto-u.ac.jp/aeasy/asym.pdf>.
- Johnstone, A.D., Alsop, C., Burge, S., Carter, P.J., Coates, A.J., Coker, A.J., Fazakerley, A.N., Grande, M., Gowen, R.A., Gurgiolo, C., Hancock, B.K., Narheim, B., Preece, A., Sheather, P.H., Winningham, J.D., Woodliffe, R.D., 1997. PEACE: A plasma electron and current experiment. *Space Sci. Rev.* 79, 351–398. <https://doi.org/10.1023/A:1004938001388>.
- Jones, S.L., Lessard, M.R., Fernandes, P.A., Lummerzheim, D., Semeter, J.L., Heinzelman, C.J., Lynch, K.A., Michell, R.G., Kintner, P.M., Stenbaek-Nielsen, H.C., Asamura, K., 2009. PFISR and ROPA observations of pulsating aurora. *J. Atmos. Solar Terr. Phys.* 71, 708–716. <https://doi.org/10.1016/j.jastp.2008.10.004>.
- Kennel, C.F., Edmiston, J.P., Hada, T., 1985. A Quarter Century of Collisionless Shock Research. AGU. pp. 1–36. <https://doi.org/10.1029/GM034p0001>.
- Kennel, C.F., Petschek, H.E., 1966. Limit on stably trapped particle fluxes. *J. Geophys. Res.* 71, 1–28. <https://doi.org/10.1029/JZ071i001p00001>.
- Klein, L.W., Burlaga, L.F., 1982. Interplanetary magnetic clouds at 1 AU. *J. Geophys. Res.* 87, 613–624. <https://doi.org/10.1029/JA087iA02p00613>.
- Lakhina, G.S., Hajra, R., Tsurutani, B.T., 2021. Geomagnetically induced currents. In: Gupta, H.K. (Ed.), *Encyclopedia of Solid Earth Geophysics*. Springer International Publishing, pp. 523–527. https://doi.org/10.1007/978-3-030-58631-7_245.
- Landau, L.D., Lifshitz, E.M., 1960. *Electrodynamics of Continuous Media*, 2nd ed. Pergamon Press, New York.
- Li, X., Baker, D.N., Temerin, M., Cayton, T.E., Reeves, E.G.D., Christensen, R.A., Blake, J.B.,Looper, M.D., Nakamura, R., Kanekal, S.G., 1997. Multisatellite observations of the outer zone electron variation during the November 3–4, 1993, magnetic storm. *J. Geophys. Res.* 102, 14123–14140. <https://doi.org/10.1029/97JA01101>.
- Liou, K., Newell, P.T., Sibeck, D.G., Meng, C.I., Brittnacher, M., Parks, G., 2001. Observation of IMF and seasonal effects in the location of auroral substorm onset. *J. Geophys. Res.* 106, 5799–5810. <https://doi.org/10.1029/2000JA003001>.
- Lui, A.T.Y., 2000. Do we understand the inner magnetotail dynamics during substorms? *Adv. Space Res.* 25, 2389–2394. [https://doi.org/10.1016/S0273-1177\(99\)00528-1](https://doi.org/10.1016/S0273-1177(99)00528-1).
- Meng, C.I., Mauk, B., McIlwain, C., 1979. Electron precipitation of evening diffuse aurora and its conjugate electron fluxes near the magnetospheric equator. *J. Geophys. Res.* 84, 2545–2558. <https://doi.org/10.1029/JA084iA06p02545>.
- Meredith, N.P., Thorne, R.M., Horne, R.B., Summers, D., Fraser, B.J., Anderson, R.R., 2003. Statistical analysis of relativistic electron energies for cyclotron resonance with EMIC waves observed on CRRES. *J. Geophys. Res.* 108, 1250. <https://doi.org/10.1029/2002JA009700>.
- Meurant, M., Gérard, J.C., Blockx, C., Coumans, V., Hubert, B., Connors, M., Lyons, L.R., Donovan, E., 2005. Comparison of intense nightside shock-induced precipitation and substorm activity. *J. Geophys. Res.* 110, A07228. <https://doi.org/10.1029/2004JA010916>.
- Morettin, P.A., 2014. Ondas e ondaletas: da análise de Fourier à análise de ondaletas de séries temporais. EDUSP.
- Newell, P.T., Gjerloev, J.W., 2011a. Evaluation of SuperMAG auroral electrojet indices as indicators of substorms and auroral power. *J. Geophys. Res.* 116, A12211. <https://doi.org/10.1029/2011JA016779>.
- Newell, P.T., Gjerloev, J.W., 2011b. Substorm and magnetosphere characteristic scales inferred from the SuperMAG auroral electrojet indices. *J. Geophys. Res.* 116, A12232. <https://doi.org/10.1029/2011JA016936>.
- Onsager, T., Grubb, R., Kunches, J., Matheson, L., Speich, D., Zwicky, R. W., Sauer, H., 1996. Operational uses of the GOES energetic particle detectors. In: Washwell, E.R. (Ed.), *GOES-8 and Beyond*. International Society for Optics and Photonics. SPIE, pp. 281–290. <https://doi.org/10.1117/12.254075>.
- Rankine, W.J.M., 1870. XV. On the thermodynamic theory of waves of finite longitudinal disturbance. *Phil. Trans. Royal Soc.* 160, 277–288. <https://doi.org/10.1098/rstl.1870.0015>.
- Rees, M.H., 1963. Auroral ionization and excitation by incident energetic electrons. *Planet. Space Sci.* 11, 1209–1218. [https://doi.org/10.1016/0032-0633\(63\)90252-6](https://doi.org/10.1016/0032-0633(63)90252-6).
- Rees, M.H., 1964. Note on the penetration of energetic electrons into the earth's atmosphere. *Planet. Space Sci.* 12, 722–725. [https://doi.org/10.1016/0032-0633\(64\)90236-3](https://doi.org/10.1016/0032-0633(64)90236-3).
- Rème, H., Bosqued, J.M., Sauvaud, J.A., Cros, A., Dandouras, J., Aoustin, C., Bouyssou, J., Camus, T., Cuvilo, J., Martz, C., Médale, J. L., Perrier, H., Romefort, D., Rouzaud, J., D'Uston, C., Möbius, E., Crocker, K., Granoff, M., Kistler, L.M., Popecki, M., Hovestadt, D., Klecker, B., Paschmann, G., Scholer, M., Carlson, C.W., Curtis, D. W., Lin, R.P., McFadden, J.P., Formisano, V., Amata, E., Bavassano-CATTANEO, M.B., Baldetti, P., Belluci, G., Bruno, R., Chionchio, G., Di Lellis, A., Shelley, E.G., Ghielmetti, A.G., Lennartsson, W., Korth, A., Rosenbauer, H., Lundin, R., Olsen, S., Parks, G.K., McCarthy, M., Balsiger, H., 1997. The Cluster ion spectrometry (CIS) experiment. *Space Sci. Rev.* 79, 303–350. <https://doi.org/10.1023/A:1004929816409>.
- Remya, B., Tsurutani, B.T., Reddy, R.V., Lakhina, G.S., Hajra, R., 2015. Electromagnetic cyclotron waves in the dayside subsolar outer magnetosphere generated by enhanced solar wind pressure: EMIC wave coherency. *J. Geophys. Res.* 120, 7536–7551. <https://doi.org/10.1002/2015JA021327>.
- Richardson, I.G., Cane, H.V., 2010. Near-earth interplanetary coronal mass ejections during solar cycle 23 (1996–2009): Catalog and summary of properties. *Solar Phys.* 264, 189–237. <https://doi.org/10.1007/s11207-010-9568-6>.
- Rostoker, G., Akasofu, S.I., Foster, J., Greenwald, R., Kamide, Y., Kawasaki, K., Lui, A., McPherron, R., Russell, C., 1980. Magnetospheric substorms—definition and signatures. *J. Geophys. Res.* 85, 1663–1668. <https://doi.org/10.1029/JA085iA04p01663>.
- Semeter, J., Kamalabadi, F., 2005. Determination of primary electron spectra from incoherent scatter radar measurements of the auroral E region. *Radio Sci.* 40, RS2006. <https://doi.org/10.1029/2004RS003042>.
- Smith, E.J., 1985. Interplanetary Shock Phenomena Beyond 1 AU. AGU. pp. 69–83. <https://doi.org/10.1029/GM035p0069>.
- Souza, A.M., Echer, E., Bolzan, M.J.A., Hajra, R., 2016. A study on the main periodicities in interplanetary magnetic field B_z component and geomagnetic AE index during HILDCAA events using wavelet

- analysis. *J. Atmos. Solar Terr. Phys.* 149, 81–86. <https://doi.org/10.1016/j.jastp.2016.09.006>.
- Souza, A.M., Echer, E., Bolzan, M.J.A., Hajra, R., 2018. Cross-correlation and cross-wavelet analyses of the solar wind IMF B_z and auroral electrojet index AE coupling during HILDCAAs. *Ann. Geophys.* 36, 205–211. <https://doi.org/10.5194/angeo-36-205-2018>.
- Østgaard, N., Tsyganenko, N.A., Mende, S.B., Frey, H.U., Immel, T.J., Fillingim, M., Frank, L.A., Sigwarth, J.B., 2005. Observations and model predictions of substorm auroral asymmetries in the conjugate hemispheres. *Geophys. Res. Lett.* 32, L05111. <https://doi.org/10.1029/2004GL022166>.
- Summers, D., Ni, B., Meredith, N.P., 2007. Timescales for radiation belt electron acceleration and loss due to resonant wave-particle interactions: 2. Evaluation for VLF chorus, ELF hiss, and electromagnetic ion cyclotron waves. *J. Geophys. Res.* 112, A04207. <https://doi.org/10.1029/2006JA011993>.
- Swift, D.W., 1978. Mechanisms for the discrete aurora — A review. *Space Sci. Rev.* 22, 35–75. <https://doi.org/10.1007/BF00215813>.
- Tanskanen, E.I., 2009. A comprehensive high-throughput analysis of substorms observed by IMAGE magnetometer network: Years 1993–2003 examined. *J. Geophys. Res.* 114, A05204. <https://doi.org/10.1029/2008JA013682>.
- Tanskanen, E.I., Pulkkinen, T.I., Viljanen, A., Mursula, K., Partamies, N., Slavin, J.A., 2011. From space weather toward space climate time scales. *J. Geophys. Res.* 116, A00I34. <https://doi.org/10.1029/2010JA015788>, Substorm analysis from 1993 to 2008.
- Thorne, R.M., Kennel, C.F., 1971. Relativistic electron precipitation during magnetic storm main phase. *J. Geophys. Res.* 76, 4446–4453. <https://doi.org/10.1029/JA076i019p04446>.
- Thorne, R.M., Ni, B., Tao, X., Horne, R.B., Meredith, N.P., 2010. Scattering by chorus waves as the dominant cause of diffuse auroral precipitation. *Nature* 467, 943–946. <https://doi.org/10.1038/nature09467>.
- Thorne, R.M., Smith, E.J., Burton, R.K., Holzer, R.E., 1973. Plasmaspheric hiss. *J. Geophys. Res.* 78, 1581–1596. <https://doi.org/10.1029/JA078i010p01581>.
- Torrence, C., Compo, G.P., 1998. A practical guide to wavelet analysis. *Bull. Am. Meteo. Soc.* 79, 61–78. [https://doi.org/10.1175/1520-0477\(1998\)079<0061:APGTWA>2.0.CO;2](https://doi.org/10.1175/1520-0477(1998)079<0061:APGTWA>2.0.CO;2).
- Tsurutani, B.T., Falkowski, B.J., Pickett, J.S., Santolik, O., Lakhina, G. S., 2015. Plasmaspheric hiss properties: Observations from Polar. *J. Geophys. Res.* 120, 414–431. <https://doi.org/10.1002/2014JA020518>.
- Tsurutani, B.T., Gonzalez, W.D., 1987. The cause of high-intensity long-duration continuous AE activity (HILDCAAs): interplanetary Alfvén wave trains. *Planet. Space Sci.* 35, 405–412. [https://doi.org/10.1016/0032-0633\(87\)90097-3](https://doi.org/10.1016/0032-0633(87)90097-3).
- Tsurutani, B.T., Gonzalez, W.D., Tang, F., Akasofu, S.I., Smith, E.J., 1988. Origin of interplanetary southward magnetic fields responsible for major magnetic storms near solar maximum (1978–1979). *J. Geophys. Res.* 93, 8519–8531. <https://doi.org/10.1029/JA093iA08p08519>.
- Tsurutani, B.T., Hajra, R., 2021. The interplanetary and magnetospheric causes of geomagnetically induced currents (GICs) > 10 A in the Mäntsälä Finland pipeline: 1999 through 2019. *J. Space Weather Space Clim.* 11, 23. <https://doi.org/10.1051/swsc/2021001>.
- Tsurutani, B.T., Hajra, R., 2023. Energetics of shock triggered supersubstorms (SML < -2500 nT). *Astrophys. J.* 946, 17. <https://doi.org/10.3847/1538-4357/abc143>.
- Tsurutani, B.T., Hajra, R., Echer, E., Gjerloev, J.W., 2015. Extremely intense (SML ≤ -2500 nT) substorms: isolated events that are externally triggered?. *Ann. Geophys.* 33, 519–524. <https://doi.org/10.5194/angeo-33-519-2015>.
- Tsurutani, B.T., Hajra, R., Echer, E., Lakhina, G.S., 2019. Comment on “First observation of mesosphere response to the solar wind high-speed streams” by W. Yi et al. *J. Geophys. Res.* 124, 8165–8168. <https://doi.org/10.1029/2018JA026447>.
- Tsurutani, B.T., Hajra, R., Tanimori, T., Takada, A., Remya, B., Mannucci, A.J., Lakhina, G.S., Kozyra, J.U., Shiokawa, K., Lee, L. C., Echer, E., Reddy, R.V., Gonzalez, W.D., 2016. Heliospheric plasma sheet (HPS) impingement onto the magnetosphere as a cause of relativistic electron dropouts (REDs) via coherent EMIC wave scattering with possible consequences for climate change mechanisms. *J. Geophys. Res.* 121, 10130–10156. <https://doi.org/10.1002/2016JA022499>.
- Tsurutani, B.T., Lakhina, G.S., Verkhoglyadova, O.P., Gonzalez, W.D., Echer, E., Guarneri, F.L., 2011. A review of interplanetary discontinuities and their geomagnetic effects. *J. Atmos. Solar Terr. Phys.* 73, 5–19. <https://doi.org/10.1016/j.jastp.2010.04.001>.
- Tsurutani, B.T., Lin, R.P., 1985. Acceleration of > 47 keV ions and > 2 keV electrons by interplanetary shocks at 1 AU. *J. Geophys. Res.* 90, 1–11. <https://doi.org/10.1029/JA090iA01p00001>.
- Tsurutani, B.T., Meng, C.I., 1972. Interplanetary magnetic-field variations and substorm activity. *J. Geophys. Res.* 77, 2964–2970. <https://doi.org/10.1029/JA077i016p02964>.
- Tsurutani, B.T., Smith, E.J., West, H.I., Buck, R.M., 1979. Chorus, energetic electrons and magnetospheric substorms. In: Palmadesso, P. J., Papadopoulos, K. (Eds.), *Wave Instabilities in Space Plasmas*. Springer, Netherlands, Dordrecht, pp. 55–62. https://doi.org/10.1007/978-94-009-9500-0_6.
- Uritsky, V.M., Pudovkin, M.I., 1998. Low frequency 1/f-like fluctuations of the AE-index as a possible manifestation of self-organized criticality in the magnetosphere. *Ann. Geophys.* 16, 1580–1588. <https://doi.org/10.1007/s00585-998-1580-x>.
- Vasyliunas, V.M., 1976. An overview of magnetospheric dynamics. In: McCormac, B.M. (Ed.), *Magnetospheric Particles and Fields*. Springer, Netherlands, Dordrecht, pp. 99–110. https://doi.org/10.1007/978-94-010-1503-5_10.
- Vörös, Z., Baumjohann, W., Nakamura, R., Volwerk, M., Runov, A., 2006. Bursty bulk flow driven turbulence in the earth's plasma sheet. *Space Sci. Rev.* 122, 301–311. <https://doi.org/10.1007/s11214-006-6987-7>.
- Wanliss, J.A., Showalter, K.M., 2006. High-resolution global storm index: Dst versus SYM-H. *J. Geophys. Res.* 111, A02202. <https://doi.org/10.1029/2005JA011034>.
- West, H.I., Buck, R.M., Walton, J.R., 1972. Shadowing of electron azimuthal-drift motions near the noon magnetopause. *Nature Phys. Sci.* 240, 6–7. <https://doi.org/10.1038/physci240006a0>.
- Wilken, B., Axford, W.I., Daglis, I., Daly, P., GÜTTLER, W., Ip, W.H., Korth, A., Kremser, G., Livi, S., Vasyliunas, V.M., Woch, J., Baker, D., Belian, R.D., Blake, J.B., Fennell, J.F., Lyons, L.R., Borg, H., Fritz, T.A., Gliem, F., Rathje, R., Grande, M., Hall, D., Kecsuemü-ÉTY, K., McKenna-LAWLOR, S., Mursula, K., Tanskanen, P., Pu, Z., Sandahl, I., Sarris, E.T., Scholer, M., Schulz, M., SØRASS, F., Ullaland, S., 1997. RAPID – the imaging energetic particle spectrometer on Cluster. *Space Sci. Rev.* 79, 399–473. <https://doi.org/10.1023/A:1004994202296>.
- Zhou, X., Tsurutani, B.T., 2001. Interplanetary shock triggering of nightside geomagnetic activity: Substorms, pseudobreakups, and quiescent events. *J. Geophys. Res.* 106, 18957–18967. <https://doi.org/10.1029/2000JA003028>.